Heliyon 6 (2020) e05369

Contents lists available at ScienceDirect

Heliyon

journal homepage: www.cell.com/heliyon

Research article

Twin Support Vector Regression for complex millimetric wave propagation environment

Anis Charrada [a,*], Abdelaziz Samet [b]

[a] SERCOM-Labs, EPT Carthage University, 2078, La Marsa, Tunis, Tunisia
[b] INRS, EMT Center, 800 de la Gauchetière W., Suite 6900, Montreal, QC, H5A 1K6, Canada

ARTICLE INFO

Keywords:
Electrical engineering
Applied computing
Signal processing
Wireless network
Communication system
Computer-aided engineering
Twin Support Vector Regression
Complex propagation environment
DWT
Wireless InSite
60 GHz band

ABSTRACT

In this article, an effective millimetric wave channel estimation algorithm based on Twin Support Vector Regression (TSVR) is proposed. This algorithm exploits Discrete Wavelet Transform (DWT) in order to denoise samples in learning phase and then enhance fitting performance. An indoor complex conference room environment full of furniture and electronic equipments is adopted for experiments. Through the proposed approach, channel frequency responses are directly estimated using the Orthogonal Frequency Division Multiplexing (OFDM) reference symbol pattern by solving two quadratic programming problems in order to improve generalization aptitude and computational speed. We consider in this work a Channel Impulse Response (CIR) of 60 GHz multipath transmission system generated by the "Wireless InSite" ray tracer by Remcom. The numerical experiments confirm the performance of the proposed approach compared to other conventional algorithms for several configuration scenarios with and without mobility.

1. Introduction

An extensive insight about the 60 GHz millimeter-Wave (mmWave) channel has been accrued and an excessive deal of work has been accomplished through the previous few years, in the direction of developing 5G wireless networks in indoor environments and evolving mmWave communication systems for commercial requests [1], [2], [3]. Accordingly, the Federal Communications Commission (FCC) assigned 7 GHz in the band of 57 to 64 GHz for unlicensed employment [4].

In fact, the high frequencies are related to both benefits and drawbacks. At 60 GHz, high propagation loss really categorizes a set of small-range applications, nevertheless it additionally incomes condensed frequency reuse designs [5]. On the other hand, mmWave frequencies yield to slighter dimensions of Radio Frequency (RF) modules containing antennas that can be relatively directional arising with important antenna gain [6], [7], which is significantly preferred.

Interestingly, the 60 GHz radio communication is appropriate for small range and high speed data transmission purposes [8], nevertheless it hurts from a reduced amount of chance of inter-system interference than the microwave UWB (Ultra Wide Band). General public consider that the 60 GHz radio be able to discover many services in workplaces, conference rooms, domestic areas, hallways, and public library [9]. It is relevant for in-home uses like support of movable equipment, devices connection and video spread. In fact, applications can be split into several groups including, wireless Gigabit Ethernet and adhoc connections, desktop point to multipoint networks, high data rate transmission and HD-video streaming [4]. In this context, high definition uncompressed video streaming can be operated in conference room for sharing the same projector between several distributed laptops [10].

It should be noted that, there are many use cases in each of these classes based on a) the geometric area (office, residential, etc.) b) devices mobility c) presence of LOS (Line-of-Sight) component or not d) coverage range between the transmitter and the receiver [5]. Obviously, NLOS (Non-Line-of-Sight) components arise from multipath environment and especially from the existence of obstacles caused by objects or human bodies that stopped the straight propagation path [11].

Accordingly, the behavior of 60 GHz radio channel properties has been well examined in the literature. An interesting review can be found in [11], [12]. It should be noted that, around 60 GHz band, the NLOS components undergo from great fluctuation, which makes transmission challenging in NLOS locations. The antennas dimensions at 60 GHz are in centimeter or sub-centimeter and had better to be directional in order to achieve high antenna gain to decrease inter-user interference and increase the signal-to-noise ratio (SNR) [13], [14]. On the other hand,

* Corresponding author.
E-mail address: anis.charrada@gmail.com (A. Charrada).

https://doi.org/10.1016/j.heliyon.2020.e05369
Received 13 July 2020; Received in revised form 23 September 2020; Accepted 26 October 2020

and as a consequence of the huge attenuation of NLOS paths, the 60-GHz frequency is sensitive to shadowing. Thus, the directional antennas may yield it further challenging when the LOS propagation component is obstructed especially in the mobility scenarios without LOS visibility.

On the other hand, Orthogonal Frequency Division Multiplexing (OFDM) is considered as an efficient multi-carrier modulation technique and a key of the broadband communication technology since it can deliver high data rate transmission, offering high spectral efficiency and simple equalizer structure [15], [16].

In multipath environments where channels are frequency-selective, OFDM scheme splits the whole bandwidth into several overlapping narrowband subchannels in order to decrease the symbol rate. In fact, each subcarrier bandwidth in the OFDM symbol is small enough dealing with flat fading in the frequency selective channel. This narrow band feature of subcarriers makes the signal robust against the channel frequency-selectivity. Moreover, by introducing a cyclic prefix (CP) in front of each OFDM symbol, the inter-symbol interference (ISI) can be simply excluded. Nevertheless, the OFDM system performance can be affected by random noise acting like external non parametric disturbance [17], timing synchronization, movement speed and channel estimation [18]. So that, it is crucial to improve the design of channel estimators to reach an appropriate reception quality.

The literature on selective channels estimation shows a variety of approaches. Linear minimum mean square error (LMMSE) [19], Discrete Fourier transform based technique [20] and basis expansion model-based channel estimation [21] have been widely investigated. Current research on OFDM systems is focused on adaptive weighted averaging estimator [22]. However, most of the previous studies do not take into account the complex millimetric-wave propagation environment and little attention has been paid to the nonlinearities exhibited by the multipath channel in the 60 GHz band transmission system.

In this direction, it is crucial to increase the overall system performance by operating an original nonlinear channel estimation approach.

Support Vector Machine (SVM) is an inspiring machine learning tool based on Vapnik-Chervonenkis (VC) dimensional theory and statistical learning theory (SLT) that has been recognized as one of the most powerful process for classification and regression problems [23]. Support Vector Regression (SVR), progressed from SVM, is relevant for nonlinear situation by the application of the kernel trick.

In the literature, some SVR algorithms have been proposed. Wu et al. proposed in [24] a feature selection approach based on TSVR. Melki et al. [25] examined multi-target regression and provided some models for multiple-outputs problems. Anand et al. [26] studied the pinball loss function in the SVR algorithm. In [27], authors examined the Lagrangian SVR problems. Additionally, authors in [28] proposed a K-nearest neighbor TSVR method applicable for regression problems with clustering samples, but not suitable for time series data such as the case of channel estimation.

To the best of our knowledge, Twin SVR based on Discrete Wavelet Transform denoising process has not been proposed to estimate a real use-case multipath channel in complex millimetric wave propagation environment into an OFDM system as proposed in this paper. In the line with this trend, the main contributions of our work are summarized as follows.

1. The paper proposes a new Twin SVR approach that can enhance both generalization performance and computational speed by solving two quadratic programming problems simultaneously (time-domain and frequency-domain problems). The proposed solution introduces a denoising process in learning stage based on Discrete Wavelet Transform which is appropriate for dealing with time-series characteristics such as mmWave wireless channel parameters. The denoising process consists of reducing the effect of outliers expected to take part in the received reference signal touched by noise.
2. This article focuses on the major challenge of scattered pilot pattern in an OFDM system for a 60 GHz multipath channel in an indoor scenario of complex conference room full of electronic equipments and furniture with and without mobility. Thus, the estimation process of the mmWave channel, treated as a strong nonlinear system, is performed under the complex Twin SVR structure in order to improve the regression performance and enhance the channel estimation accuracy.
3. We take into consideration a real use-case scenario characterized by a proved Channel Impulse Response (CIR) of a 60 GHz wireless communication system generated by the “Wireless InSite” ray tracer by Remcom [29].

This article is organized as follows. Section 2 briefly presents the system model. The Twin SVR approach based on Discrete Wavelet Transform is proposed in section 3. Section 4 describes the experimental results, and section 5 finishes the work with some concluding remarks.

Notations: $(\cdot)^{-1}$, $(\cdot)^T$ and $(\cdot)^H$ mention the inverse, transpose and transpose conjugate, respectively.

2. System model

Take into consideration a baseband equivalent model of an OFDM system with N subcarriers subject to fast fading time-varying channel as shown in Fig. 1.

The transmitted series of QAM constellation $X(k)$ are parsed into N-size blocks of frequency-domain symbols before applying the N-point IFFT (Inverse Fast Fourier Transform) in order to obtain the time-domain sequence. A cyclic prefix (CP) of length M that is equal to or larger than the channel order L is then inserted at the head of each block in order to avoid the inter-block interference (IBI). At this point, the time-domain signal $x(n)$ can be transferred in serial form over the multipath channel. The sequence $x(n)$ can be represented as the following form:

$$x(n) = \frac{1}{\sqrt{N}} \sum_{k=0}^{N-1} X(k) e^{j2\pi nk/N}, \tag{1}$$

with $n = -M, ..., N-1$. It is worth noting that the wireless transmissions undergo multipath fading propagation due to scattering and reflection of the transmitted signal. The multipath fading affects modulated symbols in terms of rotations and attenuations. Each resolvable path stands for a superposition of scattered rays that arrive at the receiver almost simultaneously with a common propagation delay. Each ray is distinguished by its own complex gain and time delay as described later in the experimental results section.

At the receiver side, after removing CP, the time-domain received signal $y(n)$ can be shown as follows:

$$y(n) = \sum_{l=0}^{L} h_l(n) x(n-l) + \kappa(n), \tag{2}$$

with $\kappa(n)$ stands for zero-mean additive white Gaussian noise (AWGN) with variance σ_n^2 and $h_l(n)$ represents the lth baseband-equivalent time-varying channel impulse response at time n.

On the other hand, equation (2) can be stated as a matrix form as follows:

$$\mathbf{y} = \mathbf{h}\mathbf{F}^{-1}\mathbf{X} + \boldsymbol{\kappa} = \mathbf{h}\mathbf{x} + \boldsymbol{\kappa}, \tag{3}$$

with $\mathbf{y} = [y(0), y(1), ..., y(N-1)]^T$, $\mathbf{x} = [x(0), x(1), \dots, x(N-1)]^T$, $\mathbf{X} = [X(0), X(1), \dots, X(N-1)]^T$ and $\boldsymbol{\kappa} = [\kappa(0), \kappa(1), ..., \kappa(N-1)]^T$. Note that, $\mathbf{y}, \mathbf{x}, \mathbf{X}, \boldsymbol{\kappa} \in \mathbb{C}^N$. Furthermore, $\mathbf{F}^{-1}$ consists of an N-point Inverse Discrete Fourier Transform (IDFT) matrix and $\mathbf{h} \in \mathbb{C}^{N \times N}$ stands for the channel matrix which can be represented as the following expression:

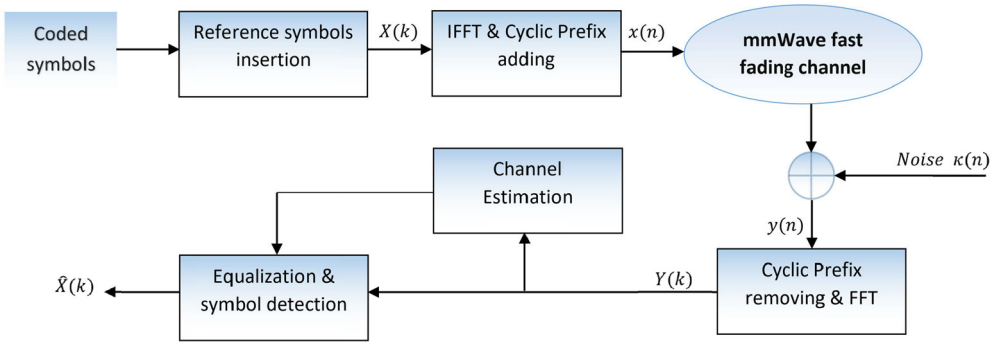

Fig. 1. Baseband equivalent model of an OFDM system.

$$\mathbf{h}=\begin{bmatrix} h_0(0) & \cdots & h_L(0) & \cdots & h_1(0) \\ \vdots & \ddots & & \ddots & \vdots \\ \vdots & & & \mathbf{0} & h_L(L-1) \\ h_L(L+1) & \cdots & h_0(L+1) & & \mathbf{0} \\ & \ddots & & \ddots & \\ \mathbf{0} & & h_L(N-1) & \cdots & h_0(N-1) \end{bmatrix}. \tag{4}$$

Note that the entry of the IDFT ($\mathbf{F}^{-1}$) and DFT ($\mathbf{F}$) matrices can be expressed respectively as

$$[\mathbf{F}^{-1}]_{n,k} = (1/\sqrt{N})\, e^{j2\pi nk/N} \tag{5}$$

$$[\mathbf{F}]_{n,k} = (1/\sqrt{N})\, e^{-j2\pi nk/N}. \tag{6}$$

After accomplishing Fourier transform on both parts of (4), we get the following expressions:

$$\mathbf{Fy} = \mathbf{FhF}^{-1}\mathbf{X} + \mathbf{F}\boldsymbol{\kappa} \tag{7}$$

$$\mathbf{Y} = \mathbf{HX} + \mathbf{F}\boldsymbol{\kappa}, \tag{8}$$

with $\mathbf{Y} = [Y(0), Y(1), \ldots, Y(N-1)]^T \in \mathbb{C}^N$ denotes the frequency-domain received signal. Additionally, $\mathbf{H} = \mathbf{FhF}^{-1} \in \mathbb{C}^{N\times N}$ symbolizes the channel matrix in frequency-domain including Inter-Carrier-Interference (ICI) caused by the time-varying channel, which components can be expressed as follows:

$$\mathbf{H}(s,q) = \frac{1}{N}\sum_{l=0}^{L} e^{-j2\pi sl/N} \sum_{n=0}^{N-1} h_l(n) e^{-j2\pi(s-q)n/N}, \tag{9}$$

with $s, q = 0, 1, \ldots, N-1$. It should be noted that $\mathbf{H}$ can be split into two portions, one amount representing the basic diagonal components $\mathbf{H}_{dg} \in \mathbb{C}^{N\times N}$ and the other representing the non-diagonal components $\mathbf{H}_{ndg} \in \mathbb{C}^{N\times N}$ corresponding to ICI elements. Thus, equations (7) can be explained as the following simplified forms:

$$\mathbf{Y} = \mathbf{H}_{dg}\mathbf{X} + \mathbf{H}_{ndg}\mathbf{X} + \mathbf{F}\boldsymbol{\kappa} \tag{10}$$

$$= diag(\mathbf{X})\mathbf{H}'_{dg} + \mathbf{H}_{ndg}\mathbf{X} + \mathbf{F}\boldsymbol{\kappa}, \tag{11}$$

where $diag(\cdot)$ indicates the diagonal operator. Moreover, the column vector $\mathbf{H}'_{dg} \in \mathbb{C}^N$ represents the components taken from the diagonal matrix $\mathbf{H}_{dg}$ and the quantity ($\mathbf{H}_{ndg}\mathbf{X}$) symbolizes the ICI components.

At the end of the receiver side, least-squares equalization is performed since it represents the least complex equalizer in order to assure real time transmission. The receiver detection operation recovers the best estimate of the modulated stream at the receiver. The main aspects of channel estimation and symbol detection are detailed in the next section.

3. Twin SVR mmWave channel estimation

Without loss of generality, Twin SVR is an extension of the supervised machine learning SVC (Support Vector Classification) to regression tool, which was proposed by Peng in [30]. In this way, TSVR represents an appropriate process for nonlinear system applications due to kernel mapping capabilities.

In this section, a novel TSVR approach based on 2D-wavelet transform denoising training signals is proposed for mmWave deep fast fading channel.

3.1. TSVR-DWT statement

Taking into account the training set $\mathbf{S} = \{(\mathbf{t}_1, o_1), (\mathbf{t}_2, o_2), \ldots, (\mathbf{t}_m, o_m)\}$, with $\mathbf{t}_i \in \mathbb{R}^2$ and $o_i \in \mathbb{R}$, $i = 1, 2, \ldots, m$. Afterwards, the input matrix of the training data can be denoted as $\mathbf{T} = (\mathbf{t}_1, \mathbf{t}_2, \ldots, \mathbf{t}_m)^T \in \mathbb{R}^{m\times 2}$ and the output vector can be stated as $\mathbf{O} = (o_1, o_2, \ldots, o_m)^T \in \mathbb{R}^m$. It should be noted that the first and second columns of $\mathbf{T}$ describe the time and frequency-domain positions of the training samples, respectively. Alternatively, the outputs represent the Least-Squares (LS) estimated channel responses.

In our proposed technique, the considered OFDM symbols contain reference and data symbols, where reference symbols are inserted equidistantly in both time and frequency directions.

The positions of reference symbols are described as $(n\Delta_t)$, $n = 0, 1, \ldots, N_t - 1$, with N_t and Δ_t stand for the number of reference symbols and reference symbol interval in time-domain, respectively. Additionally, the transmitting reference subcarrier positions in each OFDM symbol are denoted as $(m\Delta_f)$, $m = 0, 1, \ldots, N_f - 1$, with Δ_f indicates the reference interval in frequency-domain and N_f symbolizes the number of reference symbols per OFDM symbol.

In this context, consider the transmitting reference matrix expressed as $\mathbf{X}_r = diag(X(n\Delta_t, m\Delta_f)) \in \mathbb{C}^{N_tN_f\times N_tN_f}$. According to (10), the estimated channel frequency responses at reference subcarriers can be obtained by applying Least-Squares criterion as follows:

$$\hat{\mathbf{H}}_r = (\mathbf{X}_r)^{-1}\mathbf{Y}_r, \tag{12}$$

with $\hat{\mathbf{H}}_r = \hat{\mathbf{H}}(n\Delta_t, m\Delta_f) \in \mathbb{C}^{N_t\times N_f}$ represent the estimated channel frequency responses at reference positions $(n\Delta_t, m\Delta_f)$ and $\mathbf{Y}_r = \mathbf{Y}(n\Delta_t, m\Delta_f) \in \mathbb{C}^{N_t\times N_f}$ stands for the received reference vector.

3.1.1. DWT principle

Discrete Wavelet Transform (DWT) is a type of time-scale or time-frequency signal representation. Specifically, wavelet theory is appropriate for short-term time series processing since it allows the inspection of localized signal fluctuations inside the non-stationary time series. For clarity, DWT can provide time and frequency-domains decomposition of the signal simultaneously in contrast with Fourier Transform which only provides a frequency-domain decomposition ignoring the time resolution [31].

A wavelet has to fulfill only two mathematical requirements: orthogonalization and normalization conditions. Thus, a wavelet must have zero mean and finite energy. A series of wavelet can be calculated by the following equation:

$$\theta_{a,k} = \frac{1}{\sqrt{a}}\theta\left(\frac{x-k}{a}\right), \tag{13}$$

with θ symbolizes the mother wavelet and parameters a and k denote the scale and the shift of the wavelet function, respectively. There are different kinds of wavelets with several characteristics (compactness, shape and smoothness), such as Daubenhies, Mexican Hat, Morlet, etc.

3.1.2. Denoising operation

A Daubechies wavelet of the third order (db3) with a length of six is adopted in this work. The order number designates the number of vanishing moments and the length indicates the decomposition level. Hence, db3 has three vanishing moments which yield that the corresponding wavelet can approximate polynomials of degree two. The number of vanishing moments is correlated with the smoothness of the wavelet and the approximation order.

Note that, a wavelet $\boldsymbol{\theta}(t)$ is said to have p vanishing moments if it holds that [32]

$$\int_R t^m \boldsymbol{\theta}(t)\, dt = 0, \quad m = 0, 1, ..., p-1. \tag{14}$$

This yields that wavelet $\boldsymbol{\theta}(t)$ and its shifts are orthogonal to all polynomials of degrees inferior to $p-1$. Vanishing moments are also required to wavelets smoothness. Additionally, we can express the wavelets $\boldsymbol{\theta}(t)$ vanishing moments property as high pass filter vanishing moment conditions. Hence, equation (14) holds if and only if

$$\sum_{k=0}^{2n-1} k^m\, d_k = 0, \quad m = 0, 1, ..., p-1, \tag{15}$$

which d_k represent the coefficients of the high pass filter. The related low pass filter vanishing moment conditions can be obtained easily according to the alternating flip construction.

Accordingly, after the denoising operation, the estimated channel frequency responses at reference positions can be expressed as follows:

$$\hat{\mathbf{H}}_{dn} = \theta(\hat{\mathbf{H}}_r). \tag{16}$$

Thus, the predicted channel frequency responses for all OFDM data position subcarriers can be determined by the following equation:

$$\tilde{\mathbf{H}} = f(\hat{\mathbf{H}}_{dn}), \tag{17}$$

where $f(\cdot)$ symbolizes the TSVR function.

3.1.3. TSVR expression

It is worth noting that, Twin SVR is built by two bound functions: the time-domain down-bound function $f_1(\cdot)$ and the frequency-domain up-bound function $f_2(\cdot)$ corresponding to two nonparallel hyperplanes, where each hyperplane establishes their own ϵ-insensitive bound regressor. Subsequently, the global TSVR regressor represents the average of the sum of $f_1(\cdot)$ and $f_2(\cdot)$ as $f(\cdot) = \frac{1}{2}(f_1(\cdot) + f_2(\cdot))$.

Interestingly, in order to overcome the fast deep fading presented in the mmWave 60-GHz channel, we used the RBF (Radial Basis Function) known also as Gaussian kernel, due to its capability to map the input space into a possibly infinite-dimensional Hilbert output space recognized as Reproducing Kernel Hilbert Space (RKHS) through an implicit transformation $\boldsymbol{\varphi}$. So that, we simply need to calculate the Gram matrix $\boldsymbol{G}$ by performing the kernel inner product $\boldsymbol{K}$ defined by means of the input data as follows:

$$\boldsymbol{G}(1,2) = \boldsymbol{K}(\mathbf{t}_1, \mathbf{t}_2) = <\boldsymbol{\varphi}(\mathbf{t}_1), \boldsymbol{\varphi}(\mathbf{t}_2)>. \tag{18}$$

In this context, the kernel-generated down-bound and up-bound functions can be expressed in the following simplified forms, respectively:

$$f_1(\mathbf{t}) = \boldsymbol{K}(\mathbf{t}, \mathbf{T}^T)\boldsymbol{w}_1 + b_1 + e_1, \tag{19}$$

$$f_2(\mathbf{t}) = \boldsymbol{K}(\mathbf{t}, \mathbf{T}^T)\boldsymbol{w}_2 + b_2 + e_2, \tag{20}$$

where $\boldsymbol{w}_1, \boldsymbol{w}_2 \in \mathbb{C}^m$, $b_1, b_2, e_1, e_2 \in \mathbb{C}$ and $\boldsymbol{K}$ is the RBF kernel.

In order to reduce the approximation errors e_1 and e_2, we used the ε-Huber loss function introduced in [33]. Here, for simplicity reasons, we denote by $(\mathbf{t}_n^1)$ the $\mathbf{T}(n,1)$ value corresponding to the first reference symbol position at the nth line. In the same way, we denote by $(\mathbf{t}_m^2)$ the $\mathbf{T}(m,2)$ value which indicates the second reference symbol position at the mth line.

3.2. Primal problems formulations

At this point, the time-domain primal optimization functional can be stated as follows:

$$\begin{aligned} \textit{minimize} \quad & \frac{1}{2}\|\boldsymbol{w}_1\|^2 + \frac{1}{2\gamma_1}\sum_{n\in A}(\xi_n + {\xi_n}^*)^2 \\ & + C_1\sum_{n\in B}(\xi_n + {\xi_n}^*) + \frac{1}{2\gamma_1}\sum_{n\in C}(\zeta_n + {\zeta_n}^*)^2 \\ & + C_1\sum_{n\in D}(\zeta_n + {\zeta_n}^*) - \frac{1}{2}\sum_{n\in B,D}\gamma_1(C_1)^2 \end{aligned} \tag{21}$$

subject to

$$\begin{aligned} \Re\left(\hat{H}(\mathbf{t}_n^1) - \boldsymbol{w}_1^H\boldsymbol{\varphi}_1(\mathbf{t}_n^1) - b_1\right) &\le \varepsilon_1 + \xi_n \\ \Im\left(\hat{H}(\mathbf{t}_n^1) - \boldsymbol{w}_1^H\boldsymbol{\varphi}_1(\mathbf{t}_n^1) - b_1\right) &\le \varepsilon_1 + \zeta_n \\ \Re\left(-\hat{H}(\mathbf{t}_n^1) + \boldsymbol{w}_1^H\boldsymbol{\varphi}_1(\mathbf{t}_n^1) + b_1\right) &\le \varepsilon_1 + {\xi_n}^* \\ \Im\left(-\hat{H}(\mathbf{t}_n^1) + \boldsymbol{w}_1^H\boldsymbol{\varphi}_1(\mathbf{t}_n^1) + b_1\right) &\le \varepsilon_1 + {\zeta_n}^* \\ {\xi_n}^{(*)}, {\zeta_n}^{(*)} &\ge 0\,. \end{aligned} \tag{22}$$

Alternatively, the frequency-domain primal optimization problem can be expressed as the following form:

$$\begin{aligned} \textit{minimize} \quad & \frac{1}{2}\|\boldsymbol{w}_2\|^2 + \frac{1}{2\gamma_2}\sum_{m\in A'}(\xi_m + {\xi_m}^*)^2 \\ & + C_2\sum_{m\in B'}(\xi_m + {\xi_m}^*) + \frac{1}{2\gamma_2}\sum_{m\in C'}(\zeta_m + {\zeta_m}^*)^2 \\ & + C_2\sum_{m\in D'}(\zeta_m + {\zeta_m}^*) - \frac{1}{2}\sum_{m\in B',D'}\gamma_2(C_2)^2 \end{aligned} \tag{23}$$

subject to

$$\begin{aligned} \Re\left(\hat{H}(\mathbf{t}_m^2) - \boldsymbol{w}_2^H\boldsymbol{\varphi}_2(\mathbf{t}_m^2) - b_2\right) &\le \varepsilon_2 + \xi_m \\ \Im\left(\hat{H}(\mathbf{t}_m^2) - \boldsymbol{w}_2^H\boldsymbol{\varphi}_2(\mathbf{t}_m^2) - b_2\right) &\le \varepsilon_2 + \zeta_m \\ \Re\left(-\hat{H}(\mathbf{t}_m^2) + \boldsymbol{w}_2^H\boldsymbol{\varphi}_2(\mathbf{t}_m^2) + b_2\right) &\le \varepsilon_2 + {\xi_m}^* \\ \Im\left(-\hat{H}(\mathbf{t}_m^2) + \boldsymbol{w}_2^H\boldsymbol{\varphi}_2(\mathbf{t}_m^2) + b_2\right) &\le \varepsilon_2 + {\zeta_m}^* \\ {\xi_m}^{(*)}, {\zeta_m}^{(*)} &\ge 0\,, \end{aligned} \tag{24}$$

where $n = 1, \cdots, N_t$, $m = 1, \cdots, N_f$, with ξ_n, ${\xi_n}^*$ and ξ_m, ${\xi_m}^*$ indicate slack variables for errors with real positive and negative values in time and frequency-domains, respectively. In addition, ζ_n, ${\zeta_n}^*$ and ζ_m, ${\zeta_m}^*$ symbolize slack variables for errors with imaginary positive and negative values in time and frequency-domains, respectively. Parameters $C_{(1,2)}$ and $\gamma_{(1,2)}$ supervise basically the compromise between losses and regularization in time and frequency-domains, respectively.

$\{A, B, C, D\}$ and $\{A', B', C', D'\}$ denote the series of points described in time and frequency-domains by:
$\{A, A'\}$: quadratic region covering real values of errors;
$\{B, B'\}$: linear region covering real values of errors;
$\{C, C'\}$: quadratic region covering imaginary components of errors;
$\{D, D'\}$: linear region covering imaginary components of errors.

3.3. Lagrangian optimization

It should be noted that the solution of the minimization problems (21) and (23) constrained to (22) and (24) consists of constructing the following Lagrangian and then annulling its partial derivatives:

$$
\begin{aligned}
L_g &= \frac{1}{2}\left\|\boldsymbol{w}_{(1,2)}\right\|^2 + \frac{1}{2\gamma_{(1,2)}}\sum_{n,m}\left(\xi_{(n,m)}+\xi_{(n,m)}{}^*\right)^2 \\
&+C_{(1,2)}\sum_{n,m}\left(\xi_{(n,m)}+\xi_{(n,m)}{}^*\right)+\frac{1}{2\gamma_{(1,2)}}\sum_{n,m}\left(\zeta_{(n,m)}+\zeta_{(n,m)}{}^*\right)^2 \\
&+C_{(1,2)}\sum_{n,m}\left(\zeta_{(n,m)}+\zeta_{(n,m)}{}^*\right)-\frac{1}{2}\sum_{n,m}\gamma_{(1,2)}C_{(1,2)}^2 \\
&-\sum_{n,m=1}^{N_{(t,f)}}\left(\beta_{(n,m)}\xi_{(n,m)}+\beta_{(n,m)}{}^*\xi_{(n,m)}{}^*\right)-\sum_{n,m=1}^{N_{(t,f)}}\left(\lambda_{(n,m)}\zeta_{(n,m)}+\lambda_{(n,m)}{}^*\zeta_{(n,m)}{}^*\right) \\
&+\sum_{n,m=1}^{N_{(t,f)}}\alpha_{R,(n,m)}^{(1,2)}\left[\Re\left(\hat{H}(\mathbf{t}_{(n,m)}^{(1,2)})-\boldsymbol{w}_{(1,2)}^H\boldsymbol{\varphi}_{(1,2)}(\mathbf{t}_{n,m}^{(1,2)})-b_{(1,2)}\right)-\varepsilon_{(1,2)}-\xi_{(n,m)}\right] \\
&+\sum_{n,m=1}^{N_{(t,f)}}\alpha_{I,(n,m)}^{(1,2)}\left[\Im\left(\hat{H}(\mathbf{t}_{(n,m)}^{(1,2)})-\boldsymbol{w}_{(1,2)}^H\boldsymbol{\varphi}_{(1,2)}(\mathbf{t}_{n,m}^{(1,2)})-b_{(1,2)}\right)-j\varepsilon_{(1,2)}-j\xi_{(n,m)}\right] \\
&+\sum_{n,m=1}^{N_{(t,f)}}\alpha_{R,(n,m)}^{(1,2)}{}^*\left[\Re\left(-\hat{H}(\mathbf{t}_{(n,m)}^{(1,2)})+\boldsymbol{w}_{(1,2)}^H\boldsymbol{\varphi}_{(1,2)}(\mathbf{t}_{n,m}^{(1,2)})+b_{(1,2)}\right)\right. \\
&\left.-\varepsilon_{(1,2)}-\xi_{(n,m)}{}^*\right] \\
&+\sum_{n,m=1}^{N_{(t,f)}}\alpha_{I,(n,m)}^{(1,2)}{}^*\left[\Im\left(-\hat{H}(\mathbf{t}_{(n,m)}^{(1,2)})+\boldsymbol{w}_{(1,2)}^H\boldsymbol{\varphi}_{(1,2)}(\mathbf{t}_{n,m}^{(1,2)})+b_{(1,2)}\right)\right. \\
&\left.-j\varepsilon_{(1,2)}-j\zeta_{(n,m)}{}^*\right], \qquad (25)
\end{aligned}
$$

where Lagrange multipliers are subject to $\alpha_{R,(n,m)}^{(1,2)}$, $\alpha_{I,(n,m)}^{(1,2)}$, $\beta_{(n,m)}$, $\lambda_{(n,m)}$, $\alpha_{R,(n,m)}^{(1,2)}{}^*$, $\alpha_{I,(n,m)}^{(1,2)}{}^*$, $\beta_{(n,m)}{}^*$, $\lambda_{(n,m)}{}^* \geq 0$ and $\xi_{(n,m)}$, $\zeta_{(n,m)}$, $\xi_{(n,m)}{}^*$, $\zeta_{(n,m)}{}^* \geq 0$. As a result, the optimal weights in time and frequency-domains can be expressed respectively as follows:

$$\boldsymbol{w}_1 = \sum_{n=1}^{N_t}\psi_n^1\boldsymbol{\varphi}_1(\mathbf{t}_n^1), \qquad (26)$$

$$\boldsymbol{w}_2 = \sum_{m=1}^{N_f}\psi_m^2\boldsymbol{\varphi}_2(\mathbf{t}_m^2), \qquad (27)$$

where variables ψ_n^1 and ψ_m^2 can be explained by

$$\psi_n^1 = (\alpha_{R,n}^1 - \alpha_{R,n}^{1\,*}) + j(\alpha_{I,n}^1 - \alpha_{I,n}^{1\,*}), \qquad (28)$$

$$\psi_m^2 = (\alpha_{R,m}^2 - \alpha_{R,m}^{2\,*}) + j(\alpha_{I,m}^2 - \alpha_{I,m}^{2\,*}), \qquad (29)$$

where $(\alpha_{R,n}^1, \alpha_{R,n}^{1\,*}, \alpha_{I,n}^1, \alpha_{I,n}^{1\,*})$ and $(\alpha_{R,m}^2, \alpha_{R,m}^{2\,*}, \alpha_{I,m}^2, \alpha_{I,m}^{2\,*})$ denote multipliers for real and imaginary residual components in time and frequency-domains, respectively.

3.4. Dual problems representation

It is more relevant for us to present our considered nonlinear SVM framework as a compact-form matrix-format. So that, the dual problems in time and frequency-domains can be described as follows:

$$
\begin{aligned}
\textit{maximize} \quad & -\frac{1}{2}\boldsymbol{\psi}^{(1,2)H}\left(\mathbf{G}_{(1,2)}+\gamma_{(1,2)}\mathbf{I}\right)\boldsymbol{\psi}^{(1,2)}+\Re\left(\boldsymbol{\psi}^{(1,2)H}\mathbf{Y}_r\right) \\
& -\left(\boldsymbol{\alpha}_{\boldsymbol{R}}^{(1,2)}+\boldsymbol{\alpha}_{\boldsymbol{R}}^{(1,2)*}+\boldsymbol{\alpha}_{\boldsymbol{I}}^{(1,2)}+\boldsymbol{\alpha}_{\boldsymbol{I}}^{(1,2)*}\right)\mathbf{1}\varepsilon_{(1,2)}, \qquad (30)
\end{aligned}
$$

subject to

$$0 \leq \alpha_{R,(n,m)}^{(1,2)}, \alpha_{R,(n,m)}^{(1,2)}{}^*, \alpha_{I,(n,m)}^{(1,2)}, \alpha_{I,(n,m)}^{(1,2)}{}^* \leq C_{(1,2)} \qquad (31)$$

with $\boldsymbol{\psi}^{(1,2)} = [\psi_{(1,1)}^{(1,2)}, \cdots, \psi_{N_{(t,f)}}^{(1,2)}]^T$. We note also that $\mathbf{I}$ and $\mathbf{1}$ correspond to identity matrix and all ones vector, respectively. Furthermore, $\boldsymbol{\alpha}_{\boldsymbol{R}}^{(1,2)}$ and $\boldsymbol{\alpha}_{\boldsymbol{I}}^{(1,2)}$ refer to real and imaginary dual variables vectors in time and frequency-domains, respectively.

It is straightforward to show that the weights solution can be determined by optimizing the formulation (30) with respect to variables $\alpha_{R,(n,m)}^{(1,2)}, \alpha_{R,(n,m)}^{(1,2)}{}^*, \alpha_{I,(n,m)}^{(1,2)}, \alpha_{I,(n,m)}^{(1,2)}{}^*$ and afterward substituting into (26) and (27), respectively.

3.5. TSVR solution

As a result, the down-bound $f_1(\cdot)$ and up-bound $f_2(\cdot)$ functions can be established according to equations (19) and (20). Consequently, the Twin SVR regressor can be concluded by averaging the sum of these two functions as it has been stated above.

From this we can summarize the TSVR algorithm as follows:

Input: Reference symbols matrix at the transmitter and its position vector; the received reference symbols vector; the appropriate SVR parameters.

Output: The predicted frequency response of all subcarriers.

process:

1. Calculate channel frequency response at reference subcarriers by (Eq. (12)).
2. Apply Discrete Wavelet Transform (DWT) to denoise the estimated channel frequency responses at reference positions by (Eq. (16)).
3. Solve the dual problem expressed by (Eq. (30)).
4. Substitute the obtained solution into (Eq. (26)) to obtain the optimal weights in time-domain.
5. Determine the time-domain down-bound function $f_1(\cdot)$ by (Eq. (19)).
6. Repeat 1-5 once, the frequency-domain up-bound function $f_2(\cdot)$ can be obtained simultaneously according to (Eq. (20)).
7. Obtain the TSVR solution by averaging the sum of $f_1(\cdot)$ and $f_2(\cdot)$.
8. Frequency response of all subcarriers in OFDM symbols can be determined by (Eq. (17)).

4. Experimental results

In this section, we consider a Channel Impulse Response (CIR) of a 60 GHz wireless communication system generated by the "Wireless InSite" ray tracer by Remcom [29]. The CIR is provided and simulated for a use-case indoor scenario of a complex conference room full of electronic equipments and furniture. The received power levels and phase values of the multipath components incoming at the receiver are delivered at the output of the ray tracer as a function of time for a corresponding receiver sensitivity threshold.

Fig. 2 shows the Rx power and phase versus Time of Arrival (ToA) for a complex conference room scenario with receiver sensitivity thresholds (a) −80 dBm and (b) −100 dBm, respectively. Accordingly, we consider an OFDM system with $N = 1024$ subcarriers. The movement speed is 0/3 (m/s) and various types of modulation schemes QPSK, 16-QAM, 64-QAM and 128-QAM are performed.

In order to determine the effects of movement speed and multipath on channel frequency response, two use-case scenario simulations are established.

Fig. 3 displays the channel frequency response at subcarriers in several OFDM symbols under multipath number being 41 (S= −80 dBm) and 195 (S= −100 dBm) for movement speed equal to 0 and 3 m/s, respectively. It is straightforward to show that the multipath effect can cause deep frequency-domain fading. At the same time, multipath can be seen as a source of diversity. Additionally, the movement speed can cause Inter-Carrier-Interference (ICI), especially for faster movement.

We note that computer simulations are implemented in a Matlab R2017b environment on a PC. Accordingly, the well-chosen of parameters is fundamental to the performance of the SVM-based algorithms.

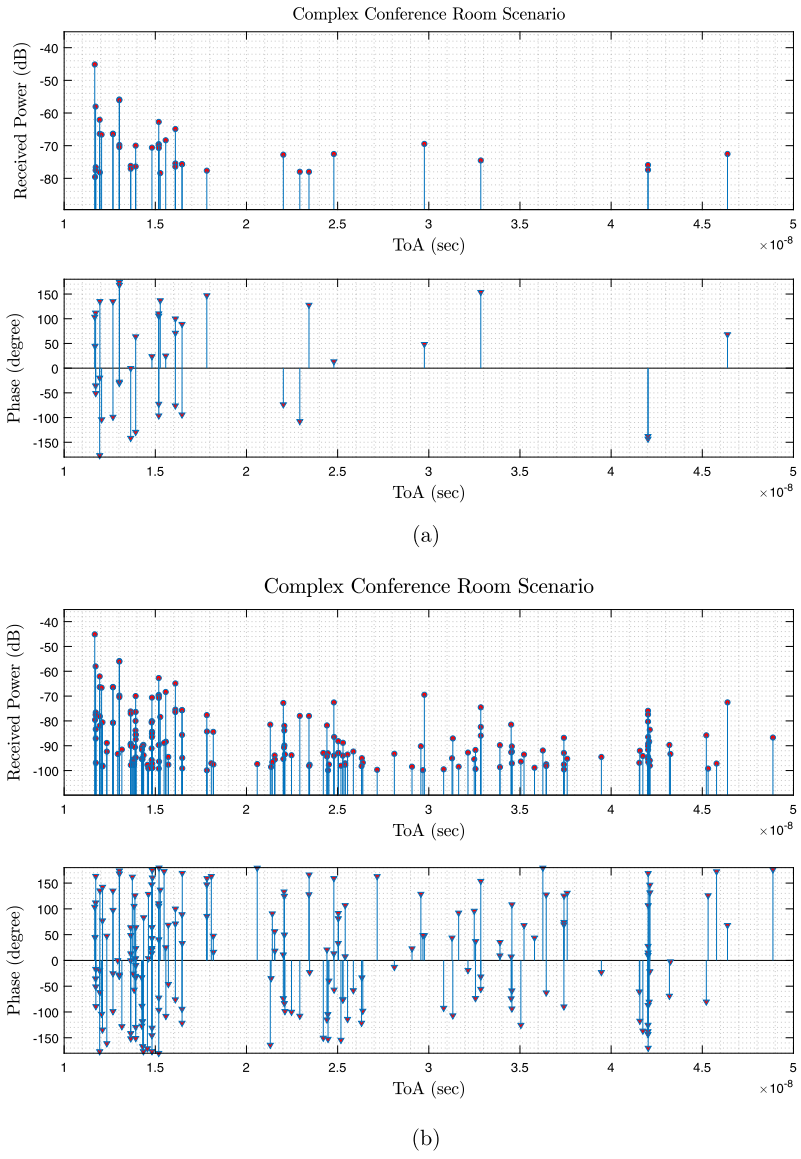

Fig. 2. Rx power and phase vs. time for a complex conference room scenario with receiver sensitivity thresholds (a) −80 dBm (41 paths) and (b) −100 dBm (195 paths), respectively.

Interestingly, we adequately select parameter values in this paper by the grid search methodology from the set of values $\{10^i | i = -5, -4, \cdots, 5\}$. The Twin SVR algorithm implementation under MATLAB uses quadratic programming (*quadprog* function in Optimization Toolbox) with the functions *buffer* and *kron* for fast calculation of kernel matrix. Alternatively, the channel estimation performance based on DWT-TSVR and other approaches are evaluated by some selected criteria. The widely studied criteria are the SNR (Signal-to-Noise Ratio) and BER (Bit Error Rate).

Fig. 4 presents the BER performance vs. SNR (varying from −10 to 30 dB at a step size of 5 dB) under multipath number being 195 and receiver sensitivity threshold equal to −100 dBm for 64-QAM modulation scheme and different movement speed (0 and 3 m/s). We compare the BER variation of the proposed algorithm with linear and cubic interpolation estimation, BEM-based estimation, LMMSE estimation LS-SVR estimation, K-nearest TSVR and perfect estimation in the presence of additive white Gaussian noise.

It can be easily seen that the behavior of the proposed approach outperforms other interpolation and estimation techniques in the sense of BER by achieving the smallest values and thus giving the best channel frequency response estimation. Accordingly, the BER performance of the proposed approach presents good fitting ability, specifically for nonlinear regression cases, due to its generalization capability and effectiveness of the denoising procedure based on Discrete Wavelet Transform to filter the noises in the training samples and then to track the rapid channel fluctuations.

Note that movement speed υ, receiver sensitivity threshold S and modulation schemes also affect the wireless system estimation performance. So that, slow movement speed leads to better estimation quality and smaller modulation scheme order can achieve a better BER. In this context, as seen in Fig. 5, the performances in terms of BER for different modulation schemes from QPSK to 128-QAM with and without mobility for $S = -80$ dBm (Fig. 5 (a)) and $S = -100$ dBm (Fig. 5 (b)), show that best performance are achieved in low modulation order obviously for low movement speed and low receiver sensitivity threshold. It is straightforward to show, as expected, that a larger BER value occurs in high modulation order caused by significant deviation of the received OFDM data symbols. Indeed, the received symbols will be distant from its original QAM constellation locations and closer to another constellation location. Thus, a wrong decision will be caused by the quantization mechanism mainly for the 128-QAM modulation scheme where the distance between QAM constellation locations is slight.

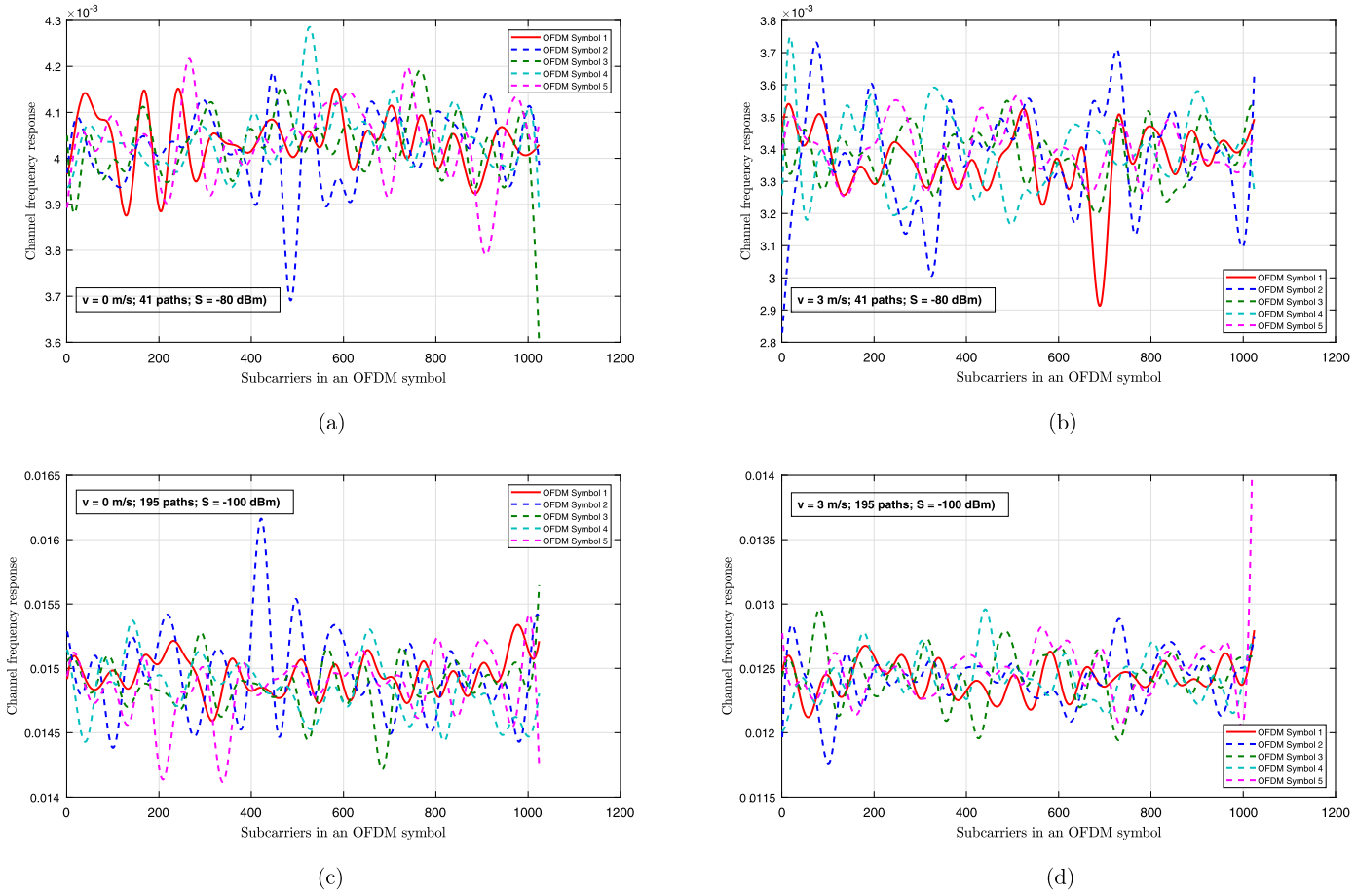

Fig. 3. Channel frequency responses at subcarriers in several OFDM symbols under multipath numbers being 41 (S = −80 dBm) and 195 (S = −100 dBm) with movement speed equal to 0 m/s and 3 m/s.

The simulation experiments listed in Table 1 displays the performance of our proposed approach for various modulation schemes (16-QAM, 64-QAM and 128-QAM) in a range of SNR varying from −10 dB to 30 dB with a step of 10 dB in terms of SSE (Sum Squared Error) with and without mobility (0 m/s and 3 m/s) under multipath numbers being 41 (S = −80 dBm) and 195 (S = −100 dBm).

The SSE criteria reveals the fitting precision and it is defined as the sum of the squared differences between each test sample and their estimated value. The presented results in Table 1 are obtained from 140 tests. It can be easily seen that good fitting ability is obtained from low modulation order (16-QAM) since the distance between QAM constellation positions is relatively large compared to 64-QAM and 128-QAM modulation schemes. Furthermore, movement speed in multipath environment causes the increase of the SSE values. Alternatively, the SSE performance of all modulation schemes listed in Table 1 presents the similar results as the BER performance. We note here that greater noise has a significant impact on TSVR-DWT, and the wavelet transform preprocessing in the training phase has limited the effect of low SNR on the system performance.

In summary, the simulation results confirm that the proposed DWT-TSVR algorithm performs better than others conventional methods in terms of good fitting abilities. Additionally, it has been proved that the introduction of the denoising item performed by the Discrete Wavelet Transform tool in the observations at the training process can clearly improve the channel estimation performance.

Table 1. SSE values of channel response for three modulation schemes.

SNR(dB)	−10	0	10	20	30
	$v = 0$ m/s, $S = -80$ dBm (41 *paths*)				
16-QAM	1206.4	120.852	12.133	1.209	0.120
64-QAM	1686.7	165.130	16.258	1.684	0.174
128-QAM	1861.1	183.680	18.529	1.858	0.187
	$v = 3$ m/s, $S = -80$ dBm (41 *paths*)				
16-QAM	4022.1	387.072	38.641	3.865	0.393
64-QAM	5533.5	540.358	55.551	5.599	0.539
128-QAM	6110.7	612.752	60.298	6.128	0.601
	$v = 0$ m/s, $S = -100$ dBm (195 *paths*)				
16-QAM	9819.9	1389.4	97.255	9.851	0.984
64-QAM	13738.2	1439.3	136.791	13.839	1.404
128-QAM	15257.1	1531.2	155.344	15.068	1.464
	$v = 3$ m/s, $S = -100$ dBm (195 *paths*)				
16-QAM	16542.2	1631.7	160.076	16.332	1.676
64-QAM	23149.1	2292.8	228.088	22.249	2.277
128-QAM	25392.1	2543.8	258.440	25.455	2.602

5. Conclusions

A novel TSVR-DWT based 60 GHz mmWave channel estimator is proposed in this paper. The multipath channel estimation is achieved in time and frequency-domains (dual domains) through the OFDM grid-introduced reference symbols. The proposed nonlinear complex Twin SVR algorithm is based on 2D-Discrete Wavelet Transform suitable for dealing with time-series characteristics such as mmWave channel parameters in order to denoise training signals and then improving regression performance and generalization ability.

This article focuses on the estimation of a mmWave fast fading channel for a use-case indoor scenario of a complex conference room full of electronic equipments and furniture with movement speed. A

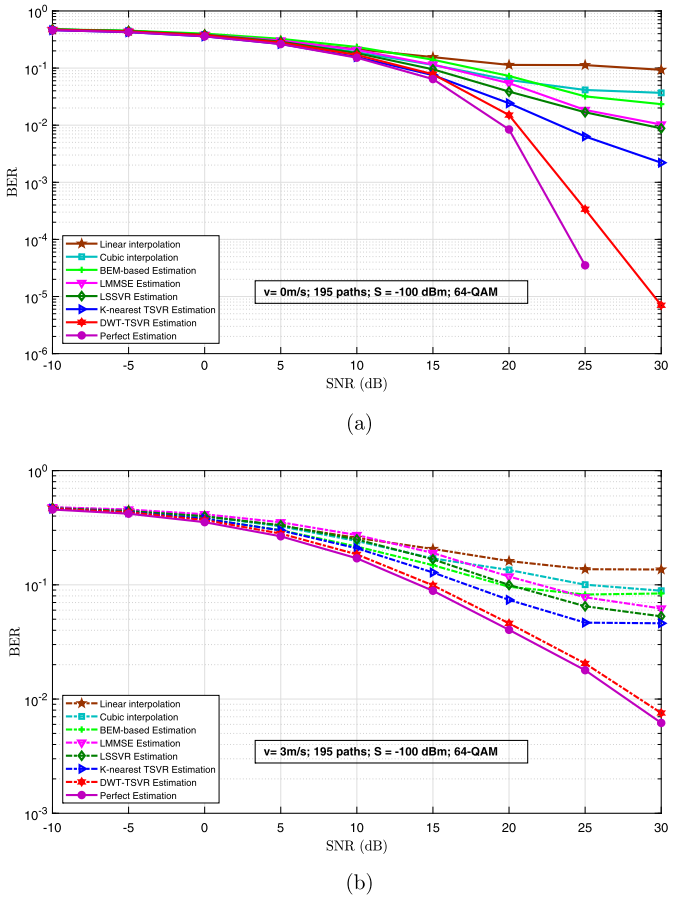

Fig. 4. BER vs. SNR for 64-QAM modulation scheme with and without mobility (a) 0 m/s and (b) 3 m/s with receiver sensitivity thresholds equal to −100 dBm (195 paths), respectively.

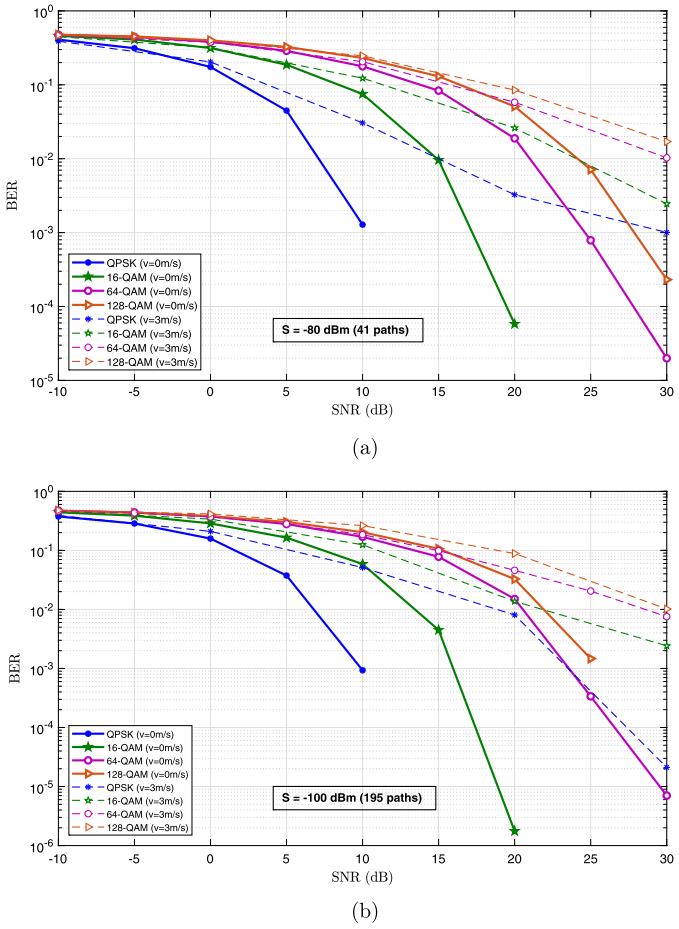

Fig. 5. BER vs. SNR for various modulation schemes with and without mobility (0 m/s and 3 m/s) under multipath numbers being 41 (S = −80 dBm) and 195 (S = −100 dBm), respectively.

Channel Impulse Response (CIR) of 60 GHz wireless communication system generated by the "Wireless InSite" ray tracer by Remcom is considered. Computational comparisons between TSVR-DWT and other conventional techniques show that the proposed TSVR-DWT has better performance of estimating the mmWave channel variations through several configuration cases.

Declarations

Author contribution statement

Anis Charrada: Conceived and designed the experiments; Performed the experiments; Analyzed and interpreted the data; Contributed reagents, materials, analysis tools or data; Wrote the paper.

Abdelaziz Samet: Conceived and designed the experiments; Performed the experiments; Analyzed and interpreted the data; Contributed reagents, materials, analysis tools or data.

Funding statement

This research did not receive any specific grant from funding agencies in the public, commercial, or not-for-profit sectors.

Declaration of interests statement

The authors declare no conflict of interest.

Additional information

No additional information is available for this paper.

Acknowledgements

The author greatly appreciate the anonymous reviewers of this paper for their valuable comments and suggestions.

References

[1] S. Li, Y. Liu, L. Lin, D. Sun, S. Yang, X. Sun, Simulation and modeling of millimeter-wave channel at 60 GHz in indoor environment for 5G wireless communication system, in: ICCEM, 2018, pp. 1–3.

[2] P. Liu, M. Di Renzo, A. Springer, Variable-N_u generalized spatial modulation for indoor los mmwave communication: performance optimization and novel switching structure, IEEE Trans. Commun. 65 (6) (2017) 2625–2640.

[3] Y. Fan, Z. Zhang, H. Li, Message passing based distributed learning for joint resource allocation in millimeter wave heterogeneous networks, IEEE Trans. Wirel. Commun. 18 (15) (2019) 2872–2885.

[4] O. Jo, S. Chang, C. Kweon, J. Oh, K. Cheun, 60 GHz wireless communication for future Wi-Fi, ICT Express (2014) 30–33, Samsung Electronics Co., Ltd. 2014.

[5] K. Guan, B. Ai, B. Peng, D. He, X. Lin, L. Wang, Z. Zhong, T. Kürner, Scenario modules, ray-tracing simulations and analysis of millimetre wave and terahertz channels for smart rail mobility, IET Microw. Antennas Propag. 12 (4) (2018) 501–508.

[6] H. Lee, E. Li, H. Jin, C. Li, K. Chin, 60 GHz wideband LTCC microstrip patch antenna array with parasitic surrounding stacked patches, IET Microw. Antennas Propag. 13 (1) (2019) 35–41.

[7] B.P.J. Zhu, S. Li, Cavity-backed high-gain switch beam antenna array for 60-GHz applications, IET Microw. Antennas Propag. 11 (12) (2017) 1776–1781.

[8] T.S. Rappaport, et al., Millimeter-wave mobile communications for 5G cellular: it will work!, IEEE Access 2013 (2013) 335–349.

[9] J. Vehmas, J. Jarvelainen, S. Nguyen, R. Naderpour, K. Haneda, Millimeter-wave channel characterization at Helsinki airport in the 15, 28, and 60 GHz bands, IEEE Access 2016 (2016) 1–5.

[10] P. Zhou, K. Cheng, X. Han, X. Fang, Y. Fang, R. He, Y. Long, Y. Liu, IEEE 802.11ay based mmWave WLANs: design, challenges and solutions, IEEE Commun. Surv. Tutor. 2018 (2018) 1–28.
[11] P. Liu, M. Di Renzo, A. Springer, Line-of-sight spatial modulation for indoor mmwave communication at 60 GHz, IEEE Trans. Wirel. Commun. 15 (11) (2016) 7373–7389.
[12] P. Liu, J. Blumenstein, N. Perovic, M. Di Renzo, A. Springer, Performance of generalized spatial modulation MIMO over measured 60ghz indoor channels, IEEE Trans. Commun. 66 (1) (2018) 133–148.
[13] B. Zhang, Y. Guo, Q. Guo, L. Wu, K. Ng, H. Wong, Y. Zhou, K. Huang, Dielectric and metallic jointly 3D-printed mmwave hyperbolic lens antenna, IET Microw. Antennas Propag. 13 (11) (2019) 1934–1939.
[14] Y. Liu, O. Bshara, I. Tekin, C. Isral, A. Hoorfar, B. Taskin, K. Dandekar, Design and fabrication of two-port three-beam switched beam antenna array for 60 GHz communication, IET Microw. Antennas Propag. 13 (9) (2019) 1438–1442.
[15] A. Sengupta, A. Alvarino, A. Catovic, L. Casaccia, Cellular terrestrial broadcast–physical layer evolution from 3GPP release 9 to release 16, IEEE Trans. Broadcast. (2020) 1–12.
[16] S. Chang, An emergence alert broadcast based on cluster diversity for autonomous vehicules in indoor environments, IEEE Access (2020) 1–4.
[17] O. Tutsoy, D.E. Barkana, H. Tugal, Design of a completely model free adaptive control in the presence of parametric, non-parametric uncertainties and random control signal delay, ISA Trans. 76 (2018) 67–77.
[18] Y. Takano, Y. Ogawa, T. Nishimura, T. Ohgane, J. Hagiwara, Channel prediction of wideband OFDM systems in a millimeter-wave band using delay-domain multipath detection, in: 2020 International Workshop on Antenna Technology (iWAT), 2020, pp. 1–4.
[19] D. Neumann, T. Wiese, W. Utschick, Learning the MMSE channel estimator, IEEE Trans. Signal Process. 66 (11) (2018) 2601–2613.
[20] F. Gu, Y. Fan, L. Wang, X. Tan, J. Wei, A universal channel estimation algorithm based on DFT smoothing filtering, IEEE Access 7 (2019) 33–39.
[21] N.M. Idrees, X. Yu, A. Springer, Optimal tracking of doubly-selective radio channels for OFDM based modern wireless systems, Phys. Commun. 35 (2019) 13–21.
[22] M. Zhang, X. Zhou, C. Wang, A novel noise suppression channel estimation method based on adaptive weighted averaging for OFDM systems, Symmetry 11 (8) (2019) 33–42.
[23] J. Xu, W. Jiang, L. Ma, M. Li, Z. Geng, Pair-υ-svr: a novel and efficient pairing nu-support vector regression algorithm, IEEE Trans. Neural Netw. Learn. Syst. 28 (11) (2017) 2503–2515.
[24] Q. Wu, H. Zhang, R. Jing, Y. Li, Feature selection based on twin support vector regression, in: 2019 IEEE Symposium Series on Computational Intelligence (SSCI), 2019, pp. 2903–2907.
[25] G. Melki, A. Cano, V. Kecman, S. Ventura, Multi-target support vector regression via correlation regressor chains, Inf. Sci. 415–416 (2017) 53–69.
[26] P. Anand, R. Rastogi, S. Chandra, A new asymmetric ϵ-insensitive pinball loss function based support vector quantile regression model, arXiv:1908.06923, 2019.
[27] S. Balasundaram, Y. Meena, A new approach for training Lagrangian support vector regression, Knowl. Inf. Syst. 49 (1) (2016) 1097–1129.
[28] S. Balasundaram, Y. Meena, K-nearest neighbor-based weighted twin support vector regression, Appl. Intell. 41 (1) (2014) 299–309.
[29] M. Tehrani Moayyed, Channel impulse response for mmwave communication, https://www.github.com/NEU-MathWorks-mmWaveProject/Channel-Impulse-Response, GitHub.
[30] X. Peng, TSVR: an efficient twin support vector machine for regression, Neural Netw. 23 (3) (2010) 365–372.
[31] L. Ortega, K. Khashanah, A neuro-wavelet model for the short-term forecasting of high frequency time series of stock returns, J. Forecast. 33 (1) (2014) 33–44.
[32] J. Karel, R. Peeters, Orthogonal matched wavelets with vanishing moments: a sparsity design approach, Circuits Syst. Signal Process. 37 (1) (2018) 3487–3514.
[33] A. Charrada, A. Samet, Estimation of highly selective channels for OFDM system by complex least squares support vector machines, AEÜ, Int. J. Electron. Commun. 66 (2012) 687–692.